

Characterization of Strain-induced Martensite and Anodic Polarization Properties of a Newly Developed Lean Duplex Stainless Steel 2002 after Tensile Deformation

Yanjun Guo¹, Jincheng Hu², Yiming Jiang¹, Jin Li^{1,*}

¹ Department of Materials Science, Fudan University, Shanghai 200433, China

² Stainless Steel Branch, Baosteel Technology Center, Baosteel Co., LTD. Shanghai 200431, China

*E-mail: corrosion@fudan.edu.cn

Received: 15 March 2016 / Accepted: 2 April 2016 / Published: 4 May 2016

Strain-induced martensite in a newly developed lean duplex stainless steel (DSS) 2002 after tensile deformation was characterized by optical metallographic microscopy, scanning electron microscopy, transmission electron microscopy, X-ray diffraction and electron backscatter diffraction techniques. Magnetic property measurement and HV hardness test of specimens with different strains were performed. The polarization curves of DSS 2002 after tensile deformation in 3.5 wt.% NaCl (pH \approx 7) and 3.5 wt.% NaCl + 0.01 mol/L HCl (pH \approx 2) were measured. The results showed that as the tensile deformation increased from 0 to 40%, the volume fraction of strain-induced martensite, the magnetization saturation and the micro-hardness values increased. The pitting potential of DSS 2002 in 3.5 wt.% NaCl solution was not greatly influenced by deformation but the critical passivation current density of specimens increased with increasing deformation. While, the pitting potential of DSS 2002 in 3.5 wt.% NaCl + 0.01 mol/L HCl decreased with the increase of tensile deformation. The effect of tensile deformation on anodic polarization properties of DSS 2002 in chloride solutions of different pH was discussed.

Keywords: duplex stainless steel; tensile deformation; strain-induced martensite; anodic polarization properties

1. INTRODUCTION

The strength and ductility of stainless steels can be remarkably improved due to transformation-induced plasticity (TRIP) effect, which has been widely investigated recently [1-10]. The TRIP mechanism is based on the transformation process of metastable austenite to martensite in fully austenitic stainless steels or metastable austenite phase of duplex stainless steels (DSSs) via uniaxial tension or cold rolling [10-25]. During plastic deformation, two different martensitic phases,

hexagonal close packed (hcp) ϵ -martensite and body centered cubic (bcc) α' -martensite can be formed [4-25]. The hcp ϵ -martensite is paramagnetic while the bcc α' -martensite is ferromagnetic. As regard to the martensitic transformations, different transformation routes take place, such as $\gamma \rightarrow \epsilon$, $\epsilon \rightarrow \alpha'$, $\gamma \rightarrow \alpha'$ and $\gamma \rightarrow \epsilon \rightarrow \alpha'$ have been proposed [4, 26]. For examples, Das et al. figured out that triple points and the intersection of shear band and grain boundary might act as nucleation sites for α' -martensite [27]. Mangonon et al. established the sequence of the martensitic transformations of UNS S304 steel during the tensile test was $\gamma \rightarrow \epsilon \rightarrow \alpha'$ [28]. Besides, recent studies reported by Fukuda et al. [29] and Huang et al. [30] revealed that both $\gamma \rightarrow \alpha'$ and $\gamma \rightarrow \epsilon \rightarrow \alpha'$ transformation routes were possible for the same stainless steel.

A number of studies of strain-induced martensitic transformation in DSSs have been reported. As examples, Herrera et al. designed a novel lean TRIP DSS with 1 GPa ultimate tensile strength and an elongation to fracture of above 60% due to the martensite transformation [31]. Zhang et al. [32] and Ran et al. [33] investigated the effect of heat treatment on TRIP effect of economical DSSs and found that the $M_{d(30/50)}$ temperature of austenite phase reduced with the annealing temperature varying from 800 to 1150 °C. Studies by Choi et al. showed the effect of nitrogen addition on the strain-induced martensitic transformation of 20Cr-0.2Ni DSS and indicated that strain-induced martensite caused TRIP effect and the elongation was up to 60% in some lean DSSs containing 0.35% N [34]. Tavares et al. studied plastic deformation via cold rolling in DSS UNS S31803 [35] and lean DSS UNS S32304 [36] and reported that UNS S32304 was much more sensitive to martensitic transformation than UNS S31803. Besides, Pramanik et al. also studied the influence of cold rolling on microstructure evolution in DSS UNS S31803 and found that the work hardening capacity of austenite was more compared to ferrite [37]. Bassani et al. reported the strain-induced martensite transformation of a cold-rolled lean DSS UNS S32101 and obtained a direct relationship between microstructure and magnetic properties [38].

In our group's previous work, a new lean DSS 2002 has been developed, of which elongation at break is able to achieve around 50% due to the TRIP effect, much higher than that of UNS S32101 [39]. However, the martensitic transformations process of DSS 2002 remains unclear. Additionally, pitting corrosion of stainless steels, acting as one of crucial localized corrosive attacks, is mainly associated with microscopic heterogeneities at a surface rather than macroscopic physical features of a component [40-41]. It is significantly dependent on metallurgical factors including the effect of alloying elements and the distribution of the secondary phases and non-metallic inclusions [42-44]. A high defect density and strain-induced martensite can be induced during plastic deformation, thus, it is of great interest to study what effect the plastic deformation has on the corrosion resistance of stainless steel. The pitting corrosion resistance of austenite stainless steels may be influenced by plastic deformation [45-47]. Nevertheless, little attention has been focused on the influence of plastic deformation on the anodic polarization properties of DSSs in chloride solutions of different pH in previous research.

In the present work, microstructure of strain-induced martensite in the novel lean TRIP DSS 2002 was characterized by scanning electron microscopy, transmission electron microscopy, X-ray diffraction and electron backscatter diffraction. Magnetic property and HV hardness of specimens with different strains were tested. The polarization curves of DSS 2002 after tensile deformation in 3.5

wt.% NaCl (pH \approx 7) and 3.5 wt.% NaCl + 0.01 mol/L HCl (pH \approx 2) were measured. The relationship between anodic polarization properties and chloride solutions of different pH with respect to tensile deformation was discussed.

2. MATERIALS AND METHODS

2.1. Materials

A newly developed novel lean DSS 2002 was studied in this work, of which the chemical composition was shown in Table 1. The material was produced as described previously [39]. The raw materials were melted in a 50 kg vacuum furnace and then cast as a single square ingot. When the oxide skin was removed, the ingot was forged into square slabs at the temperature ranging from 900 to 1200 °C with a thickness of 40 mm. The slabs were reheated at 1200 °C for 2h and hot-rolled, using a laboratory hot-rolling mill, into 4 mm thick plates and then cold-rolled into 1.5 mm. Then, the specimens were solution-treated at 1000 °C for 30 min in an arc furnace, followed by water quenching.

Table 1. Chemical composition of DSS 2002.

Element	C	Si	Mn	P	S	Cr	Ni	Mo	Cu	N
wt.%	0.031	0.32	3.45	0.01	0.004	20.53	2.08	0.31	0.34	0.17

2.2 Tensile deformation

The material for examinations was in the form of sheet-cutting steel with dimensions of 250 mm \times 30mm \times 1.5 mm. It was subjected to tensile deformation by tension with true strains 5%, 10%, 20%, 30% to 40%. Tensile deformation tests were conducted on an Instron 5985 testing machine according to BS EN ISO 6892-1:2009 [48]. Subsequently, rectangular specimens with dimension about 10 mm \times 10 mm were cut from these specimens after tensile deformations of 5%, 10%, 20%, 30% and 40% for study.

2.3. Microstructure characterization

Metallographic specimens were etched in Beraha's etching (80 mL distilled water, 20 mL hydrochloric acid and 0.3g potassium metabissulfite), which made the austenite bright and the ferrite dark. The microstructure was observed using optical metallographic microscopy (OMM) after etching. Meanwhile, a SCE Phillips XL30 FEG scanning electron microscopy (SEM) was used to investigate the microstructure of tensile specimens.

Transmission electron microscopy (TEM) was carried out on JEOL JEM 2100F with operating at 200 kV to examine the microstructure evolution of specimens under different tensile strains. TEM

foils were prepared by conventional twin-jet electro-polishing machine at the voltage of 25V in the solution composed of 10 vol.% perchloric acid and 90 vol.% ethanol at $-30\text{ }^{\circ}\text{C}$.

The X-ray diffraction (XRD) measurement was performed on a D8 ADVANCE X-ray diffractometer with DAVINCI. DESIGN using Cu $K\alpha$ ($\lambda=0.154056\text{ nm}$) radiation and operating at 40 kV and 20 mA, in the step-scan mode with a step size of 0.01 ° . The diffraction spectra have a 2θ angular range of 40 to 100 ° .

The microstructure and microtexture were also analyzed by an electron back scattering diffraction (EBSD) system attached to the FEI Quarter 400 SEM using a scan step size of $0.1\text{ }\mu\text{m}$.

2.4. Magnetic measurement and HV Hardness test

Magnetization saturation was measured by a Quantum Design vibrating sample magnetometer (VSM). Microhardness test with a loading of 100 g was performed on a HMV-2TADW microhardness tester.

2.5. Electrochemical measurements

The polarization curves of the specimens were measured using a CHI 660D electrochemical workstation. The electrochemical measurements were carried out with a three-electrode cell where a Pt foil acted as the auxiliary electrode and a saturated calomel electrode (SCE) as the reference electrode. All potentials presented in this work referred to SCE. The specimens acting as working electrodes were embedded in epoxy resin. Prior to each experiment, the working electrode was wet ground mechanically using successive grade emery papers from 180 to 2000 grit, subsequently polished with a $1.5\text{ }\mu\text{m}$ diamond paste, rinsed with acetone and ethanol and then dried in air. To avoid the crevice corrosion, interfaces between specimen and resin were sealed with silica gel sealant, and dried in air. The exposed electrode surface area was 10 mm^2 . The test solution was made up of analytical grade reagent and distilled water. Before and during the test, the electrolyte was bubbled with pure nitrogen gas (N_2) to get rid of the oxygen gas (O_2) for 30 min and maintained throughout the test.

Polarization tests were respectively performed in solutions of 3.5 wt.% NaCl ($\text{pH} \approx 7$) and 3.5 wt.% NaCl + 0.01 mol/L HCl ($\text{pH} \approx 2$) at $30\text{ }^{\circ}\text{C}$ with a scan rate of 0.1667 mV/s from -0.8 V versus SCE to the pitting potential (E_{pit}) versus SCE. The pitting potential was identified as the potential at which the current density continuously exceeded $100\text{ }\mu\text{A/cm}^2$ [49]. In addition, prior to the potentiodynamic polarization measurements, cathodic polarization at -900 mV versus SCE for 2 min was employed to deoxidize the surface of the working electrode, then followed by stabilization at open circuit potential for 30min to form stable passivation film on the specimens' surface. Each electrochemical testing was repeated at least three times, and the average data were chosen as the corrosion parameter values in this work. After tests, the microstructure of pits was observed using backscattered electron microscopy.

3. RESULTS AND DISCUSSION

3.1 Microstructure Characterization

Fig. 1 showed the typical optical microstructure of DSS 2002 without tensile deformation. It could be observed that the bright etched band-shaped austenite phase was evenly embedded in the dark etched ferrite matrix. The volume fraction of ferrite and austenite, evaluated by quantitative metallography based on the software attached to the OMM, were 0.52 ± 0.03 and 0.48 ± 0.03 , indicating that the duplex phases approximately reached balance.

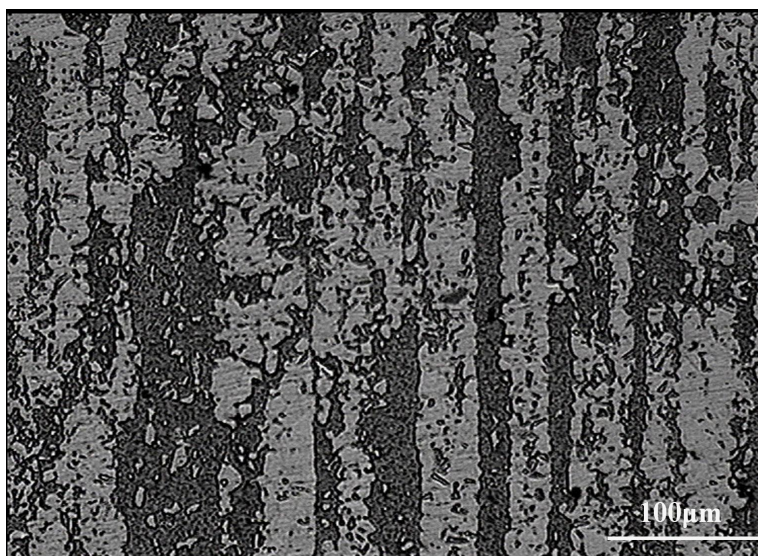


Figure 1. Optical micrograph of DSS 2002 without tensile deformation, the dark area represents ferrite while the bright representing austenite.

Fig. 2a-e demonstrated the SEM microstructure of DSS 2002 with tensile deformations of 5%, 10%, 20%, 30% and 40%. The microstructure of specimen with a portion of paralleled lath-type martensite inside the austenite island (see white circles in the image) could be detected. After 5% tensile deformation, a few martensitic variants could be seen inside the austenitic grains. When specimens were subjected to 20% deformation, microstructure of austenite was presented mostly by lath-shaped martensite with different orientations. Then, after 40% deformation, there were quite a few martensitic variants in retained austenite phase, suggesting that the amount of strain-induced martensite gradually increased with the increase of tensile deformation. Fig. 2f was the partial magnification of the dotted line circle in Fig. 2e. It was shown that the high dislocation density was introduced by tensile deformation, accompanying with the formation of strain-induced martensite. However, it should be noted that it was difficult for SEM to precisely distinguish between martensitic lathes, slip lines and deformation twins. Also, it was hard to quantitatively measure the volume fraction of martensite.

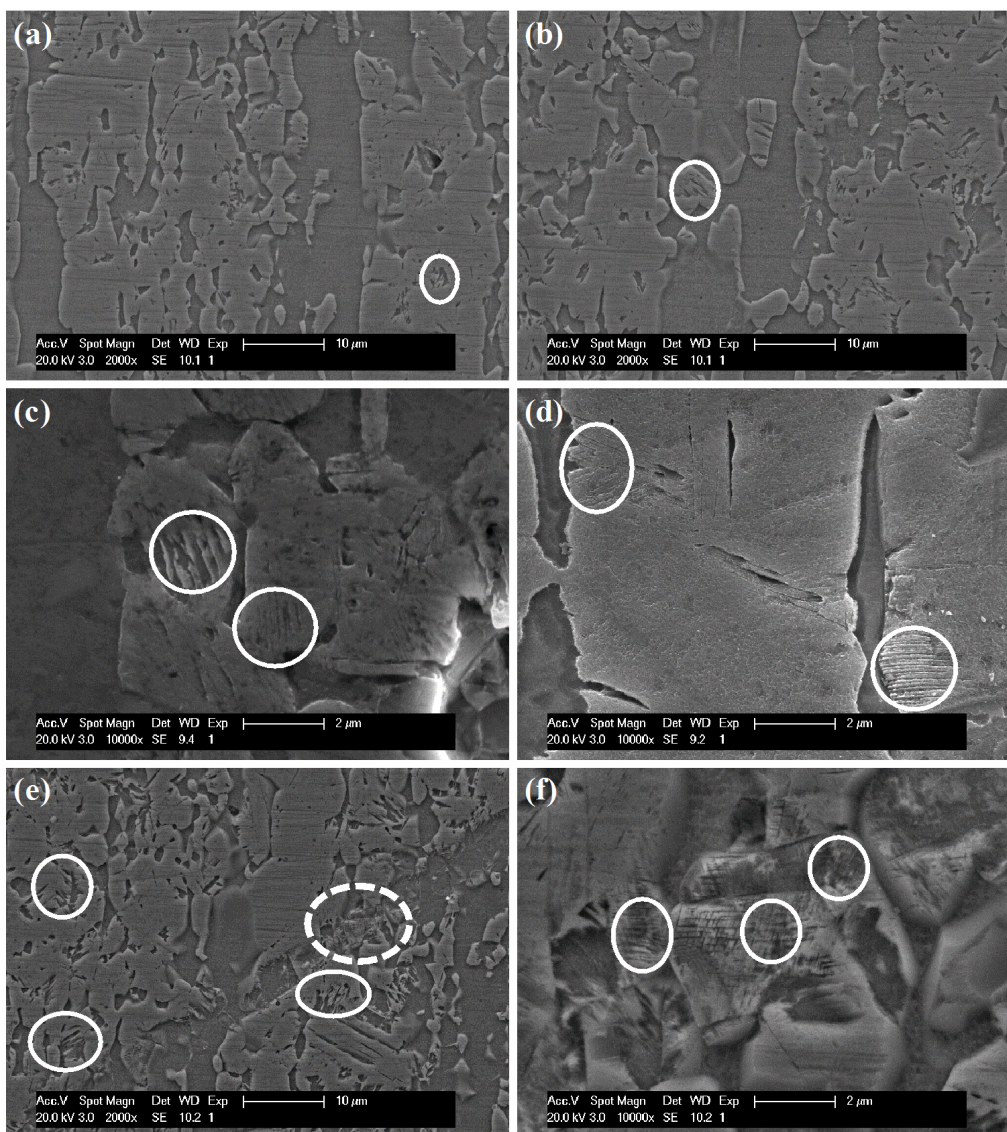


Figure 2. SEM microstructure of the specimens after different tensile deformations, (a) 5%, (b) 10%, (c) 20%, (d) 30%, (e) 40% and (f) the partial magnification of the dotted line circle in (e). The martensite portions inside the austenite phase are highlighted by solid circles.

Further metallographic studies were conducted by TEM. The representative TEM micrographs of the specimens deformed to various strains of 5%, 10% and 40% were shown in Fig. 3. It could be obviously seen that the deformation twins were formed in the specimens after 5% strain (Fig. 3a). On the basis of the diffraction pattern analysis, as shown in Fig.3a(3), the deformation bands were identified as ϵ -martensite with the zone axis of $[110]_{\gamma} // [1120]_{\epsilon}$, according with the well-known Shoji-Nishiyama relationship of close packed parallelism between austenite and ϵ -martensite. The TEM characterization of specimens deformed to 10% was revealed in Fig.3b, which showed that the α' martensite with the zone axis of $[110]_{\gamma} // [100]_{\alpha'}$ were induced. The parallel orientation relationship between austenite and α' -martensite was close to the Nishiyama-Wassermann relationship. Fig.3c showed the microstructure of specimens after 40% tensile strain. The typical lath-type α' martensite texture could be found, which was also consistent with Nishiyama-Wassermann relationship.

Consequently, it was suggested that two types of martensitic transformation mechanism occurred via the sequences of $\gamma \rightarrow \epsilon$ and $\gamma \rightarrow \alpha'$ during tensile deformation. However, the orientation relationship of strain-induced ϵ -martensite and strain-induced α' -martensite was not detected, which might be attributed to the low amount of ϵ -martensite.

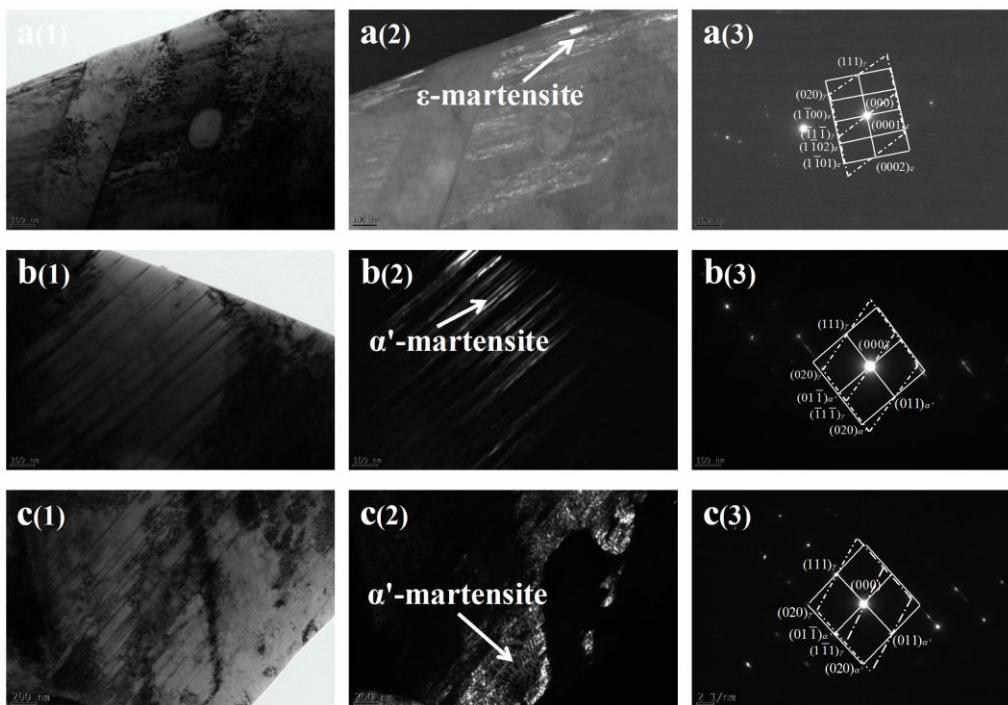


Figure 3. TEM micrographs of the specimens deformed at different strains, (a) 5%, (b) 10%, (c) 40%, and 1, 2 and 3 representing bright-field image, dark-field image and diffraction pattern analysis, respectively.

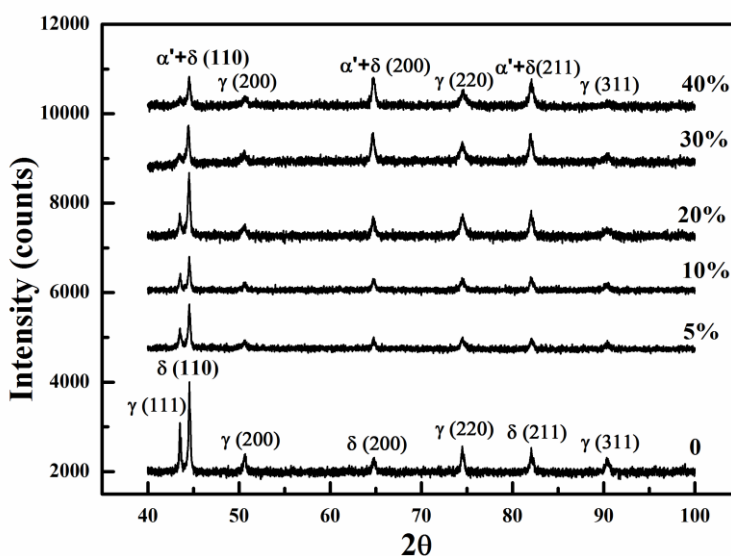


Figure 4. X-ray spectra of the specimens before and after different deformations

Fig. 4 exhibited the X-ray diffraction spectra of the specimens under different strains of 0, 5%, 10%, 20%, 30% and 40%. As could be seen, the diffraction peaks of specimens before and after deformation were both composed of face centered cubic (fcc) austenite (γ) phase and body centered cubic (bcc) phases. Based on aforementioned TEM analysis, it has been established that ϵ -martensite as one of deformation variants of austenite phase presented in the specimens after 5% strain. However, the X-ray diffraction peak of hexagonal close packed (hcp) ϵ -martensite was not observed in specimens with 5% deformation, which might be ascribed to the low-content of ϵ -martensite. In addition, it has been universally acknowledged that α' -martensite had bcc crystal structure, the same with ferrite phase (here named δ -ferrite), and it was impossible to isolate them. Thus, the bcc diffraction peaks of specimens after deformation were a combination of α' -martensite and δ -ferrite. From Fig.4, the intensities of fcc austenite diffraction peak (111), (200), (220) and (311) decreased as the tensile strain increased from 0 to 40%. The intensity of bcc diffraction peak could reflect the presence of α' -martensite, even if it did not occur uniformly for each diffraction plane. The intensity of bcc diffraction peak (200) increased with the increase of strain from 10% to 40%, revealing that the amount of α' -martensite increased. Hence, it was worthwhile to regard that α' -martensite phase might expand along a preferred-orientation plane (200) of deformed specimens.

Fig. 5 revealed the EBSD analysis of specimens subjected to 10% and 20% deformation. Herein, ferrite and austenite phases were marked with gray and blue, respectively. The green represented deformed austenite and the white was α' -martensite. It was shown that the microstructure of the specimens at 10% strain was mainly composed of a band structure of ferrite grains and a bamboo structure of austenite grains along the tensile direction. Besides, the white strain-induced α' -martensite was dotted in austenite phase, as shown in Fig. 5a. Fig. 5b displayed that the deformation proceeded to 20%, the austenite grains refined and the amount of strain-induced α' -martensite increased a lot. The amount of strain-induced α' -martensite measured by EBSD in specimens deformed at 10% strain was 2.6 vol.%, while that of 20% strain was 5.6 vol.%. Nevertheless, the content of ϵ -martensite of specimens with 5% strain was too low to be tested. In addition, the austenite of specimens with strain 30% and 40% were severely deformed and EBSD could not detect α' -martensite.

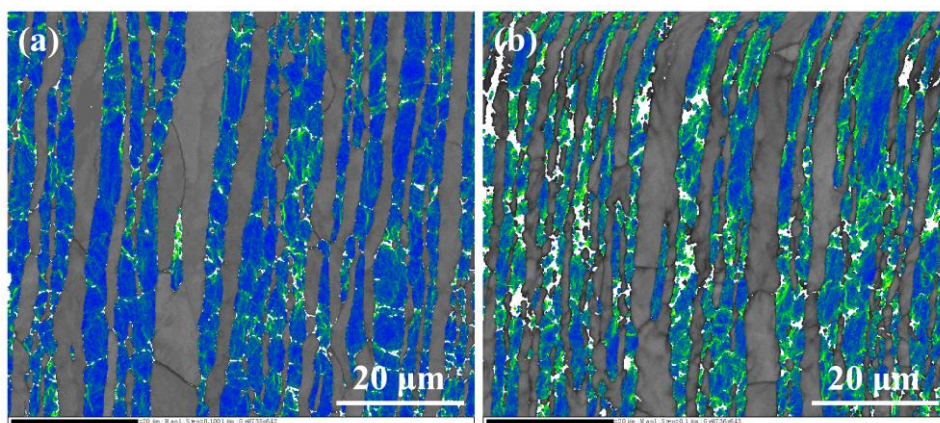


Figure 5. EBSD micrograph of the specimens subjected to tensile deformations (a) 10% and (b) 20%. The gray, blue, green and white represents ferrite, austenite, deformed austenite and strain-induced α' -martensite.

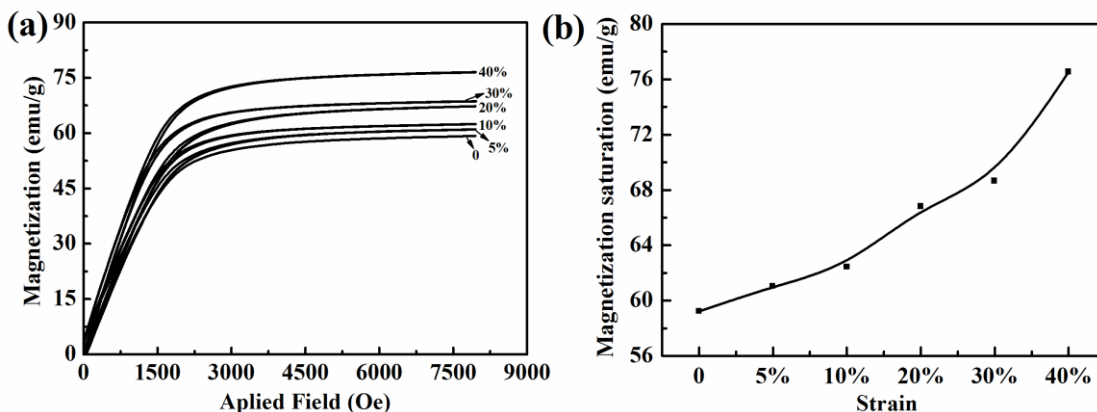


Figure 6. (a) Magnetization curves of the specimens with different tensile strains, (b) Magnetization saturation with different tensile strains

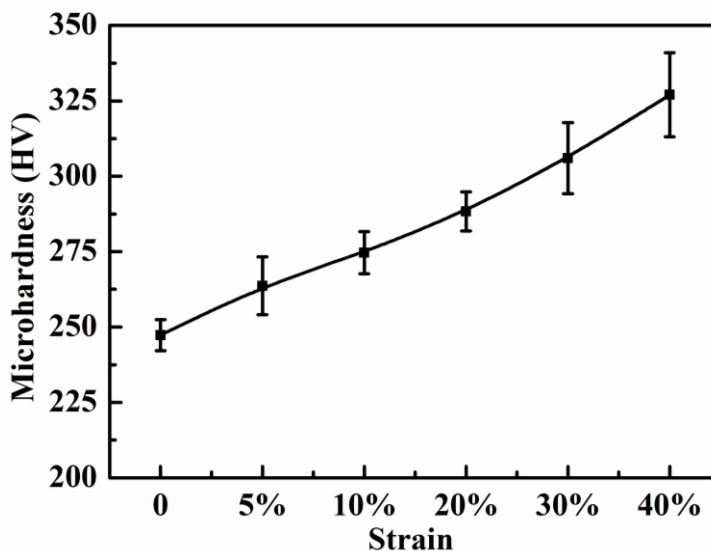


Figure 7. HV hardness with different tensile strains

3.2 Magnetic property and HV micro-hardness

The magnetization curves of specimens with different tensile strains were shown in Fig. 6a and the relevant magnetization saturation versus deformation behavior was plotted in Fig. 6b. With tensile deformation increasing from 0 to 40%, the magnetization saturation increased monotonically. The strain-induced ϵ -martensite was not engaged in discussion as it was paramagnetic, while, the amount of ferromagnetic strain-induced α' -martensite could contribute to the value of magnetization saturation. Accordingly, it could be figured out that the amount of α' -martensite increased as the strain increased from 0 to 40%. In addition to magnetic property, the micro-hardness was also tested. Fig. 7 exhibited that the Vickers hardness increased linearly from 247 to 327 with the increase of tensile strain. This might be attributed to strain hardening effect, where high local dislocation density and strain-induced martensite played a significant role [9, 12].

3.3 Anodic polarization properties

The pitting corrosion resistances of DSS 2002 with different tensile deformations in 3.5 wt.% NaCl (pH \approx 7) and 3.5 wt.% NaCl + 0.01 mol/L HCl (pH \approx 2) at 30 °C were studied by potentiodynamic polarization measurements.

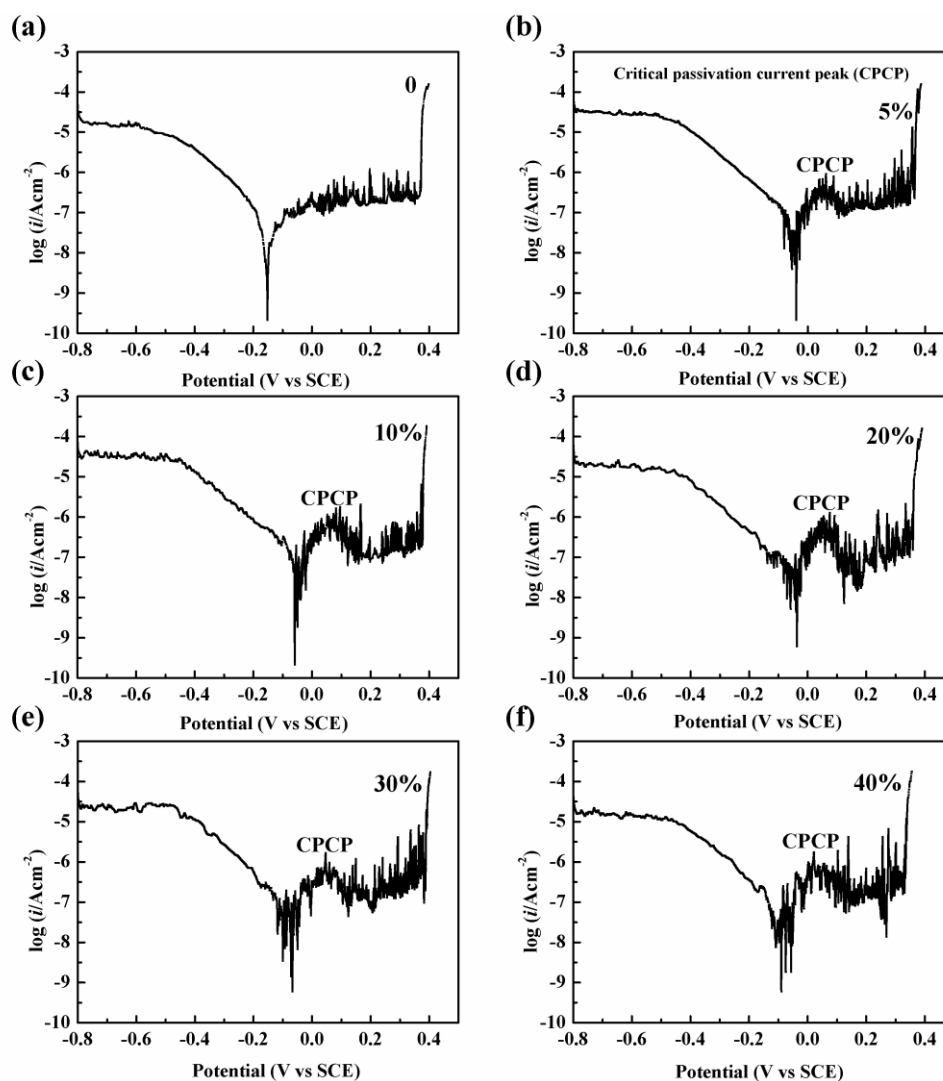


Figure 8. Potentiodynamic polarization curves for the specimens with different tensile strains in 3.5 wt.% NaCl solution, (a) 0, (b) 5%, (c) 10%, (d) 20%, (e) 30% and (f) 40%.

Fig. 8 exhibited representative polarization curves for specimens with different tensile strains in 3.5 wt.% NaCl. It could be found that there was a passivation region in the anodic branch. In the passivation range of the specimens with different tensile deformations varying from 0 to 40%, the current density increased and then decreased until the current density value reached $100 \mu\text{A}/\text{cm}^2$, revealing that samples were in an unstable passive state or in a condition where both active and passive states coexisted [50]. Besides, it also should be noted that there emerged a critical passivation current peak (CPCP) of the deformed specimens, which might be attributed to that strain-induced martensite had a high passivation current density [46]. Average corrosion parameters of polarization curves were

listed in Table 2. As could be seen, the corrosion potential (E_{corr}) of deformed specimens was higher than that of undeformed specimen. Besides, the surface geometrical feature could affect the distribution of the current density during the electrochemical reactions [51-55], which may also influence the corrosion rate.

Table 2. Average corrosion parameters of the specimens studied in 3.5 wt.% NaCl solution

Sample-strain	$E_{\text{corr}} / \text{V}$	$\log(i_{\text{corr}} / \text{A cm}^{-2})$	$\log(i_{\text{cp}} / \text{A cm}^{-2})$	$E_{\text{pit}} / \text{V}$
0	-0.143	-8.15	-6.51	0.387
5%	-0.061	-6.48	-6.17	0.382
10%	-0.080	-6.45	-5.98	0.388
20%	-0.056	-6.52	-5.89	0.385
30%	-0.087	-6.80	-5.78	0.386
40%	-0.076	-6.73	-5.53	0.383

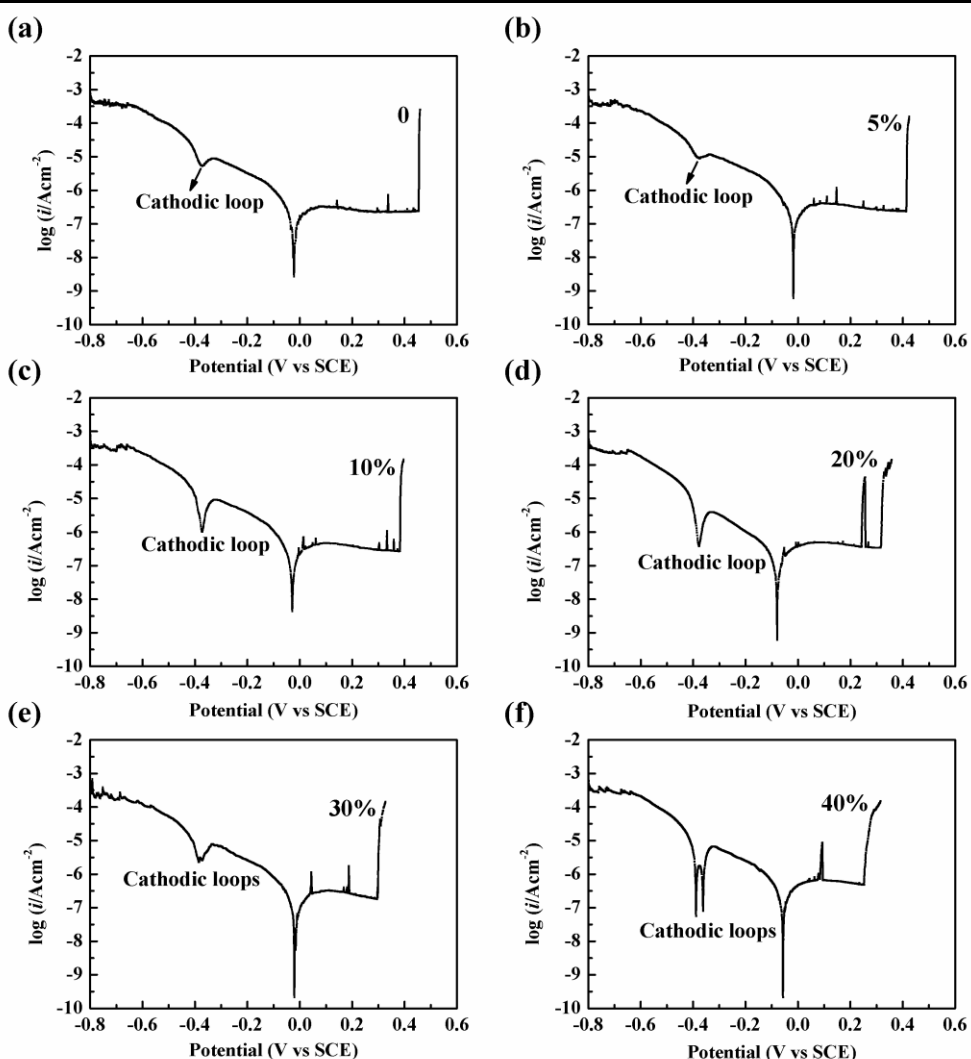


Figure 9. Potentiodynamic polarization curves for the specimens with different tensile strains in 3.5 wt.% NaCl + 0.01 mol/L HCl solution, (a) 0, (b) 5%, (c) 10%, (d) 20%, (e) 30% and (f) 40%.

The corrosion current density (i_{corr}) of deformed specimens was also higher. According to Huang et al., the corrosion potential value was approximately equal to the open circuit potential [56]. The results indicated that tensile deformation made the passivation difficult by shifting the open circuit potential in the active direction. In addition, the critical passivation peak current density (i_{cp}) of specimens increased as the tensile deformation increased from 0 to 40%. These results was in consistent with the previous research steel studied by Xu et al. that plastic deformation markedly decreased the passivity ability of UNS S304 austenitic stainless [57]. Nevertheless, the undeformed and deformed specimens exhibited similar pitting potential (E_{pit}), suggesting that the pitting corrosion resistance of DSS 2002 in neutral chloride solution remained unaffected by tensile deformation. Moura et al. also reported that no change in the pitting potential of UNS S31803 in 3.5 wt.% NaCl occurred although the martensite formed during cold deformation [58]. Thus, it could be concluded that tensile deformation made the critical passivation current density increased but it had no obvious influence on pitting potential of specimens in 3.5 wt.% NaCl solution.

The polarization curves for specimens under different tensile trains in 3.5 wt.% NaCl + 0.01 mol/L HCl were shown in Fig. 9. It could be seen that the polarization curves of acidic chloride solution showed one or two negative loops of cathodic currents, leading to two or three negative peaks.

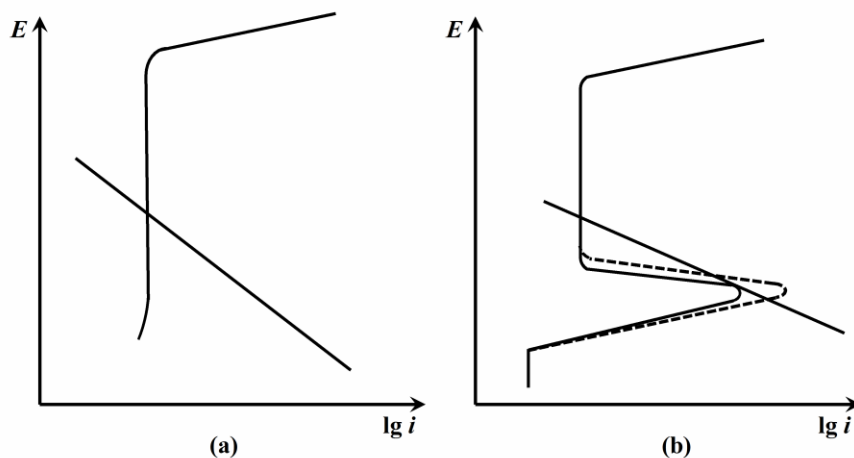
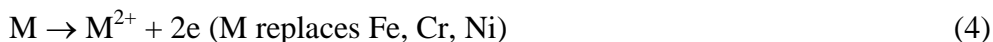


Figure 10. The simple diagrams of the real cathodic polarization curve and anodic polarization curve in chloride media (a) neutral chloride solution and (b) acidic chloride solution.

It was well known that the polarization curves measured in the experiment were apparent ones, and the anodic and cathodic currents or curves were the sum of real anodic and cathodic currents at given polarization potentials [59-63]. The simple diagrams of real cathodic polarization curve and anodic polarization curve of DSS 2002 in chloride media were displayed in Fig. 10. In neutral and acidic chloride media, two cathodic reactions possibly occurred: the oxygen reduction in neutral media or the hydrogen reduction in acid solutions, as Eq. (1-3).



The anodic reactions were mainly the iron dissolution, and other alloys dissolution, such as chromium, nickel, as shown in Eq. (4).



For DSS 2002, the neutral chloride medium was an anodic passivation system, while the acidic chloride media was an anodic active-passivation system. In the neutral chloride solution, the real anodic polarization curve and cathodic polarization curve met only once, and therefore there was one negative peak, as shown in Fig. 10a, which was in good agreement with Fig. 8. Fig. 10b indicated that two or three negative peaks might be intersected by real anodic polarization curve and cathodic polarization curve in the acidic chloride solution. Fig. 10b also illuminated that when the samples subjected to high tensile deformation, such as 30% and 40% strain, the corrosion aggravated and the active current peak increased from the solid line to the dotted line. Consequently, the number of negative peaks in the apparent polarization curve rose to three, as shown in Fig. 9.

Table 3. Average corrosion parameters of the specimens studied in 3.5 wt.% NaCl + 0.01 mol/L HCl solution.

Sample-strain	$\log(i_p / \text{A cm}^{-2})$	$E_{\text{pit}} / \text{V}$
0	-6.48	0.456
5%	-6.39	0.420
10%	-6.32	0.391
20%	-6.31	0.352
30%	-6.49	0.321
40%	-6.18	0.302

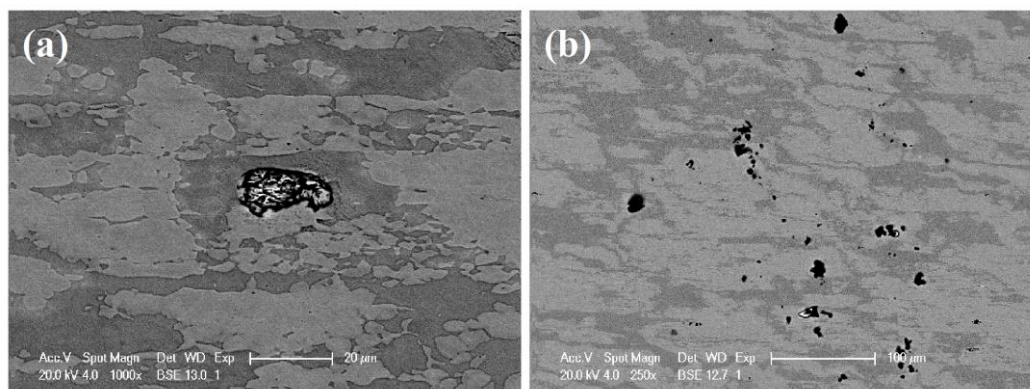


Figure 11. Morphologies of pitting attack formed on specimens with 40% strain after the potentiodynamic polarization test in chloride solutions, (a) 3.5 wt.% NaCl and (b) 3.5 wt.% NaCl + 0.01 mol/L HCl.

Due to the complexity of the polarization curve in acidic chloride solution, the corrosion potential and corrosion current could not be precisely calculated. Thus, the average corrosion parameters just including passivation current density (i_p) and pitting potential were collected in Table

3. The passivation current density (i_p) of the specimens in acidic chloride solution varied little. While, the pitting potential decreased from 0.456 to 0.302 V as the strain increased from 0 to 40%, suggesting that the pitting corrosion resistance of DSS 2002 in acidic chloride solution was deteriorated by tensile deformation and the pitting corrosion resistance of specimens decreased with the increase of strain. In conclusion, the tensile deformation had no influence on passivation of specimens in 3.5 wt.% NaCl solution + 0.01 mol/L HCl solution, but it was harmful to the pitting potential, which might be attributed to the lower hydrogen over voltage of imperfection sites introduced by tensile deformation.

The typical pitting morphologies of specimens with 40% strain after potentiodynamic polarization tests were observed using backscattered electron microscopy, as presented in Fig. 11. Fig. 11a and Fig. 11b demonstrated that the pitting morphologies of 3.5 wt.% NaCl and 3.5 wt.% NaCl + 0.01 mol/L HCl, respectively. It could be figured out that the stable pit of specimens of 40% strain was located at the boundary of ferrite phase and austenite phase after electrochemical measurement in neutral chloride solution, which further sustained that the pitting corrosion resistance was not influenced by tensile deformation. Whereas, in acidic chloride solution, many stable and metastable pits were formed in the specimens after 40% strain and most of them were located in the austenite phase, suggesting that the pitting corrosion preferentially occurred in the austenite phase. Combining the aforementioned results, it could be found that the metastable austenite phase included high dislocation density and strain-induced martensite. These dislocations might act as active sites for anodic dissolution in acidic chloride media due to the lower bonding energies at these points [64]. Consequently, the high dislocation density and strain-induced martensite were easily activated by the addition of hydrogen ion, in good accordance with the result that the pitting corrosion resistance of specimens in acidic chloride solution decreased with the increase of strain.

4. CONCLUSIONS

Strain-induced martensite in a new lean TRIP DSS 2002 has been characterized by SEM, TEM, XRD and EBSD. Magnetization saturation and micro-hardness values were tested. Anodic polarization properties were investigated in 3.5 wt.% NaCl (pH \approx 7) and 3.5 wt.% NaCl + 0.01 mol/L HCl (pH \approx 2) solutions, respectively. The main conclusions were as follows.

1. Two types of martensitic transformation mechanism occurred via the sequences of $\gamma \rightarrow \epsilon$ and $\gamma \rightarrow \alpha'$ during tensile deformation. Strain-induced α' -martensite phase might expand along a preferred-orientation plane (200).
2. The amount of strain-induced martensite increased with the increase of the strain, companying with formation of the high local dislocation density.
3. The Vickers micro-hardness increased linearly from 247 to 327 with increasing the deformation, as a result of strain hardening effect induced by strain-induced martensite and high local dislocation density.
4. In neutral chloride solution (3.5 wt.% NaCl), the pitting potential of specimens remained unaffected by tensile deformation, but the critical passivation current density of specimens increased with the strain, which might be associated with that strain-induced martensite had a higher

critical current density for passivation.

5. In acidic chloride solution (3.5 wt.% NaCl + 0.01 mol/L HCl), the passivation current density varied little but the pitting potential decreased with the increase of strain, which seemed to be related to the preferential dissolution of imperfection sites introduced by tensile deformation.

ACKNOWLEDGEMENTS

The authors acknowledge the supports of the National Natural Science Foundation of China (Grants No. 51131008, 51371053).

References

1. J. Charles, *Steel Res. Int.*, 79 (2008) 455.
2. J.O. Nilsson, *Mater. Sci. Technol.*, 8 (1992) 685.
3. J.O. Nilsson, A. Wilson, *Mater. Sci. Technol.*, 8 (1993) 545.
4. K.H. Lo, C.H. Shek, J.K.L. Lai, *Mat. Sci. Eng., R*, 65 (2009) 39.
5. G. Frommeyer, U. Brux, P. Neumann, *ISIJ Int.*, 43 (2003) 438.
6. H.F.G. de Abreu, S.S. de Carvalho, P. de Lima Neto, R.P. dos Santos, V.N. Freire, P.M. de Oliveira Silva, S.S. Maior Tavares, *Mater. Res.*, 10 (2007) 359.
7. W. Hubner, *Tribol. Int.*, 34 (2001) 231.
8. A. Weiss, H. Gutte, P.R. Scheller, *Steel Res. Int.*, 77 (2006) 727.
9. N. Tsuchida, Y. Morimoto, T. Tonan, Y. Shibata, K. Fukaura, R. Ueji, *ISIJ Int.*, 51 (2011) 124.
10. E. Ishimaru, H. Hamasaki, F. Yoshida, *J. Mater. Process. Technol.*, 223 (2015) 34.
11. Y. Li, F. Bu, W. Kan, H. Pan, *Mater. Manuf. Processes*, 28 (2013) 256.
12. M. Chen, D. Terada, A. Shibata, N. Tsuji, *Mater. Trans.*, 54 (2013) 308.
13. A. Das, P.C. Chakraborti, S. Tarafder, H.K.D.H. Bhadeshia, *Mater. Sci. Technol.*, 27 (2011) 366.
14. P. Hausild, K. Kolarik, M. Karlik, *Mater. Design*, 44 (2013) 548.
15. N. Nakada, H. Ito, Y. Matsuoka, T. Tsuchiyama, S. Takaki, *Acta Mater.*, 58 (2010) 895.
16. S.S.M. Tavares, J.M. Pardal, M.J. Gomes Da Silva, H.F.G. Abreu, M.R. Da Silva, *Mater. Character.*, 60 (2009) 907.
17. L. Zhang, S. Takahashi, Y. Kamada, *Scripta Mater.*, 57 (2007) 711.
18. W. Liu, J. He, M. Fan, P. Lu, L. Shao, *J. Mater. Sci. Technol.*, 23 (2007) 319.
19. G. Yang, C. Huang, S. Wu, Z. Zhang, *Acta Metall. Sin.*, 45 (2009) 906.
20. Z. Zhang, Q. Ran, Y. Xu, X. Yu, D. Jiang, X. Xiao, *J. Iron. Steel Res. Int.*, 21 (2014) 69.
21. J.Y. Choi, J.H. Ji, S.W. Hwang, K. Park, *Mater. Sci. Eng., A*, 528 (2011) 6012.
22. J.Y. Choi, J.H. Ji, S.W. Hwang, K. Park, *Mater. Sci. Eng., A*, 535 (2012) 32.
23. J.Y. Choi, S.W. Hwang, M.C. Ha, K. Park, *Met. Mater. Int.*, 20 (2014) 893.
24. S.S. Sohn, S. Lee, B.J. Lee, J.H. Kwak, *JOM*, 66 (2014) 1857.
25. M. Fujisawa, R. Mauchi, T. Morikawa, M. Tanaka, K. Higashida, *Tetsu to Hagane – Journal of the Iron and Steel Institute of Japan*, 100 (2014) 1140.
26. E. Nagy, V. Mertinger, F. Tranta, J. Solyom, *Mater. Sci. Eng., A*, 378 (2004) 308.
27. A. Das, S. Sivaprasad, M. Ghosh, P.C. Chakraborti, S. Tarafder, *Mater. Sci. Eng., A*, 486 (2008) 283.
28. P.L. Mangonon, G. Thomas, *Metall. Trans.*, 1 (1970) 1577.
29. T. Fukuda, T. Kakeshita, K. Kindo, *Mater. Sci. Eng., A*, 438 (2006) 212.
30. C.X. Huang, G. Yang, Y.L. Gao, S.D. Wu, S.X. Li, *J. Mater. Res.*, 22 (2007) 724.
31. C. Herrera, D. Ponge, D. Raabe, *Acta Mater.*, 59 (2011) 4653.
32. W. Zhang, J.C. Hu, *Mater. Character.*, 79 (2013) 37.

33. Q. Ran, Y. Xu, J. Li, J. Wan, X. Xiao, H. Yu, L. Jiang, *Mater. Design*, 56 (2014) 959.
34. J.Y. Choi, J.H. Ji, S.W. Hwang, K. Park, *Mater. Sci. Eng., A*, 534 (2012) 673.
35. S.S.M. Tavares, M.R. Da Silva, J.M. Pardal, H.F.G. Abreu, A.M. Gomes, *J. Mater. Process. Technol.*, 180 (2006) 318.
36. S.S.M. Tavares, J.M. Pardal, M.R. Da Silva, C.A.S. De Oliveira, *Mater. Res.-Ibero-Am. J.*, 17 (2014) 381.
37. S. Pramanik, S. Bera, S.K. Ghosh, *Steel Res. Int.*, 85 (2014) 776.
38. P. Bassani, M. Breda, K. Brunelli, I. Meszaros, F. Passaretti, M. Zanellato, I. Calliari, *Microsc. Microanal.*, 19 (2013) 988.
39. Y.J. Guo, J.C. Hu, J. Li, L.Z. Jiang, T.W. Liu, Y.P. Wu, *Materials*, 7 (2014) 6604.
40. G.S. Frankel, *J. Electrochem. Soc.*, 145 (1998) 2186.
41. C. Zhong, X. Tang, Y.F. Cheng, *Electrochim. Acta*, 53 (2008) 4740.
42. C. Zhong, F. Liu, Y.T. Wu, J.J. Le, L. Liu, M.F. He, J.C. Zhu, W.B. Hu, *J. Alloy. Compd.*, 520 (2012) 11.
43. J.J. Le, L. Liu, F. Liu, Y.D. Deng, C. Zhong, W.B. Hu, *J. Alloy. Compd.*, 610 (2014) 173.
44. Y. Li, J. Liu, Y. Deng, X. Han, W. Hu, C. Zhong, *J. Alloy. Compd.*, 673 (2016) 28.
45. L. Peguet, B. Malki, B. Baroux, *Corros. Sci.*, 49 (2007) 1933.
46. U.K. Mudali, P. Shankar, S. Ningshen, R.K. Dayal, H.S. Khatak, B. Raj, *Corros. Sci.*, 44 (2002) 2183.
47. Y. Fu, X. Wu, E. Han, W. Ke, K. Yang, Z. Jiang, *Electrochim. Acta*, 54 (2009) 1618.
48. British Standards (BS) European Norm (EN) International Organization for Standardization (ISO) 6892-1:2009, "Metallic materials Tensile testing; Part 1: Method of test at ambient temperature", European Committee for Standardization, Brüssel, 2009.
49. Chinese Industrial Standard GB/T 17899-1999, Standard Test Method for Electrochemical Pitting Potential Testing of Stainless Steels, China, 2000.
50. Z. Feng, X. Cheng, C. Dong, L. Xu, X. Li, *Corro. Sci.*, 52 (2010) 3646.
51. J. Liu, X.T. Du, Y. Yang, Y.D. Deng, W.B. Hu, C. Zhong, *Electrochem. Comm.*, 58 (2015) 6.
52. C. Zhong, W.B. Hu, Y.F. Cheng, *J. Power Sources*, 196 (2011) 8064.
53. J. Liu, W. B. Hu, C. Zhong, Y.F. Cheng, *J. Power Sources*, 223 (2013) 165.
54. X.T. Du, Y. Yang, J. Liu, B. Liu, J.B. Liu, C. Zhong, W.B. Hu, *Electrochim. Acta*, 111 (2013) 562.
55. J. Liu, C. Zhong, Y. Yang, Y.T. Wu, A.K. Jiang, Y.D. Deng, Z. Zhang, W.B. Hu, *Int. J. Hydrog. Energ.*, 37 (2012) 8981.
56. C.H. Huang, J.C. Huang, J.B. Li, J.S.C. Jang, *Mater. Sci. Eng., C*, 33 (2013) 4183.
57. C.C. Xu, G. Hu, *Anti-Corros. Methods Mater.*, 51 (2004) 381.
58. V.S. Moura, L.D. Lima, J.M. Pardal, A.Y. Kina, R.R.A. Corte, S.S.M. Tavares, *Mater. Charact.*, 59 (2008) 1127.
59. G. Song, *Corros. Sci.*, 51 (2009) 2063.
60. F. Liu, Y.D. Deng, X.P. Han, W.B. Hu, C. Zhong, *J. Alloy. Compd.*, 654 (2016) 163.
61. C. Zhong, M.F. He, L. Liu, Y.J. Chen, B. Shen, Y.T. Wu, Y.D. Deng, W.B. Hu, *Surf. Coat. Technol.*, 205 (2010) 2412.
62. C. Zhong, M. F. He, L. Liu, Y. T. Wu, Y. J. Chen, Y. D. Deng, B. Shen, W. B. Hu, *J. Alloy. Compd.*, 504 (2010) 377.
63. C. Zhong, W. B. Hu, Y. M. Jiang, B. Deng, J. Li, *J. Coat. Technol. Res.*, 8 (2011) 107.
64. K. Elayaperumal, P.K. De, J. Balachandra, *Corrosion*, 28 (1972) 269.